

Free-Energy Landscape of the Dissolution of Gibbsite at High pH

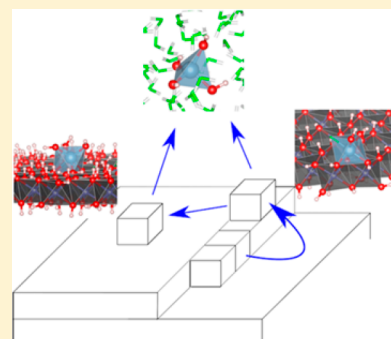
Zhizhang Shen,^{*,†} Sebastien N. Kerisit,[†] Andrew G. Stack,[‡] and Kevin M. Rosso^{*,†}

[†]Physical Sciences Division, Physical & Computational Sciences Directorate, Pacific Northwest National Laboratory, Richland, Washington 99352, United States

[‡]Chemical Science Division, Oak Ridge National Laboratory, Oak Ridge, Tennessee 37831, United States

S Supporting Information

ABSTRACT: The individual elementary reactions involved in the dissolution of a solid into solution remain mostly speculative due to a lack of direct experimental probes. In this regard, we have applied atomistic simulations to map the free-energy landscape of the dissolution of gibbsite from a step edge as a model of metal hydroxide dissolution. The overall reaction combines kink formation and kink propagation. Two individual reactions were found to be rate-limiting for kink formation, that is, the displacement of Al from a step site to a ledge adatom site and its detachment from ledge/terrace adatom sites into the solution. As a result, a pool of mobile and labile adsorbed species, or adatoms, exists before the release of Al into solution. Because of the quasi-hexagonal symmetry of gibbsite, kink site propagation can occur in multiple directions. Overall, our results will enable the development of microscopic mechanistic models of metal oxide dissolution.



The process of dissolution of a solid into solution is fundamental in nature and industry yet because of its complexity at microscopic scales remains challenging to quantitatively describe at an elementary level. While for decades it has been relatively straightforward to measure and develop mechanistic models of dissolution inferred from ion release rates and microscopic observations,^{1,2} because there are no truly direct local probes capable of resolving in both space and time the individual elementary reactions involved such models continue to be speculative. Molecular simulation methods are now approaching the power and sophistication necessary to encompass key aspects of dissolution including ion solvation/desolvation and hydrolysis, bond breaking and reformation, ion diffusion, and detachment at an explicitly described solid/solution interface.^{3–9} To treat such aspects collectively on an equal footing remains accessible primarily to classical force field molecular dynamics (MD) methods. Even so, most attempts on relatively simple ionic materials exist to date,^{3,4} and few have been developed and performed specifically for covalently bonded metal oxides.

In the present study, we use MD simulations to explore the elementary dissolution reactions of an important metal hydroxide and quantitatively assess the rate-limiting reactions at the microscopic scale. The dissolution of gibbsite (γ -Al(OH)₃) in concentrated NaOH solutions is the critical digestion step of the Bayer process used for aluminum production.^{10,11} Similar to the Bayer process, the current treatment of high-level radioactive waste (HLW) at the Hanford site, WA, U.S.A. involves leaching the sludge, which is primarily composed of gibbsite and boehmite (γ -AlOOH),^{12,13} with highly concentrated NaOH solution (e.g., 3 M) at elevated temperature (e.g., 80 °C). However, the rate of dissolution in this leaching process is much slower than

predicted, limiting the overall processing rate.¹⁴ In all cases, a detailed understanding of the gibbsite dissolution mechanism, especially at high pH, would be beneficial for process optimization.

This system is ideal as a case study for molecular simulation of metal oxide dissolution for several reasons. The overall reaction of interest is conceptually simple¹⁵



Relevant experimental data are readily available. Numerous studies^{11,16–18} have been conducted on macroscopic-scale dissolution of gibbsite in basic conditions with varying temperature, pressure, concentration, morphology, and surface area. Finally, because the gibbsite structure is a two-dimensional network of a single topologically unique octahedral Al(OH)₆ site, the effort can be focused primarily on just one site as the key dissolving nutrient from the basal plane.

Few molecular simulation strategies are available in which the output can be directly compared to macroscopic observables. Dissolution rates of step edges can usually be estimated from in situ atomic force microscopy (AFM) observations, as demonstrated in the work of Peskley et al.¹⁹ on gibbsite dissolution at pH = 3. These observed step velocities can help justify the parameters used in kinetic Monte Carlo simulations, for example, which could link the individual surface reactions to the overall experimentally observed rate.²⁰ Alternatively, recent MD simulations coupled with rare-event sampling techniques, such as metadynamics and umbrella sampling, have successfully

Received: February 13, 2018

Accepted: March 25, 2018

Published: March 26, 2018

mapped the free-energy landscape for multistep growth/dissolution reaction processes and produced accurate rates in aqueous environments.^{3,4} Here we adopt this strategy for gibbsite dissolution in order to compare the level of success attainable for a metal oxide with its prior implementation for ionic crystal dissolution.

An in situ AFM dissolution study of the gibbsite (001) basal surface at low pH revealed that dissolution proceeds by step retreat, which begins with the formation of etch pits.¹⁹ Three dominant steps bounding edge pits are (110), (100), and (010), with the first deduced to be the most stable. Identical step orientations emerge from gibbsite dissolution in highly concentrated NaOH (from our complementary experiments). The reason behind the formation and relative stability of these step edges, independent of pH, is primarily the density of Al–OH bonds along the edge direction. Because of the similar bonding topologies along these step edges, we focus our simulations on the dissolution process at a (110) step bounding an etch pit.

Metadynamics and umbrella sampling simulations with a CLAYFF-based force field²¹ are employed to map the free-energy landscapes for $\text{Al}(\text{OH})_x(\text{H}_2\text{O})_y^{3-x}$ monomer detachment from a (110) step edge at high pH (Figure 1A). The two

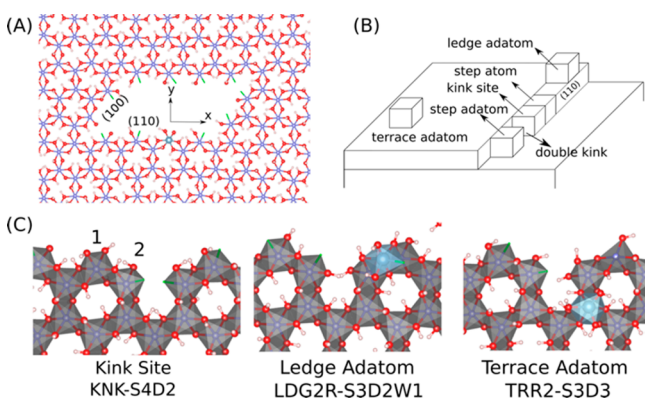


Figure 1. (A) Etch pit model on gibbsite (001). The coordinate system used in the free-energy maps is also shown. Al, O, and H atoms are shown as blue, red, and white spheres, respectively. The target Al atom on the step is shown in cyan. Water molecules are not drawn, but the Al–O_w bonds are shown as green sticks. (B) Schematic illustrating the nomenclature used for the different surface sites. (C) Atomistic models for KNK-S4D2, LDG2-S3D2W1 (blue polyhedron), and TRR2-S3D3 (blue polyhedron) sites as examples for the kink site, ledge adatom, and terrace adatom site, respectively. Kink sites 1 and 2 were deprotonated (KNK-S4D2) in kink site dissolution calculations.

basic processes of step edge dissolution, kink formation and kink propagation,²² are simulated. Simulation details and force field benchmarking can be found in the [Supporting Information](#). Because it is not easy to handle pH in molecular simulations, we adopt a strategy of representing high pH conditions by deprotonating one terminal singly bonded H₂O to Al at the step edge. The resulting step atomic species is $[\text{>Al}(\text{OH})_2]^-$, which has been theoretically determined to be the most stable site at pH > PZC.²³ In what follows, the Al sites (Figure 1B,C) are labeled by the site type (STA for a step atom site, KNK for a kink site, TRR for a terrace adatom, and LDG for a ledge adatom) and the numbers of bonds between Al and surface hydroxyls (S), between Al and dangling hydroxyls (D), and between Al and water molecules (W, omitted if no such bond exists). For example, Al at the initial step atom site is

labeled STA-S4D2, or Al at the kink site is labeled KNK-S4D2 (Figure 1C). In order to differentiate two adatom sites with the same coordination environment (e.g., S3D3), a digit identifier is used after the three-letter abbreviation (e.g., TRR2-S3D3, Figure 1C). The letters L and R are also added to the ledge adatom label (e.g., LDG2R-S3D2W1, Figure 1C) to differentiate between ledge adatom sites to the left and right of the double kink site, which show different topologies.

Three individual processes emerged from the simulations of double kink site formation at the (110) step edge: (1) displacement of Al from the step atom site to an adatom site atop the ledge, (2) migration of Al adatoms away from the ledge onto the (001) terrace, and (3) detachment of ledge/terrace adatom sites into solution.

Free-energy maps for the displacement of Al from the step edge to the left ledge are shown in Figure 2A,B. In the first

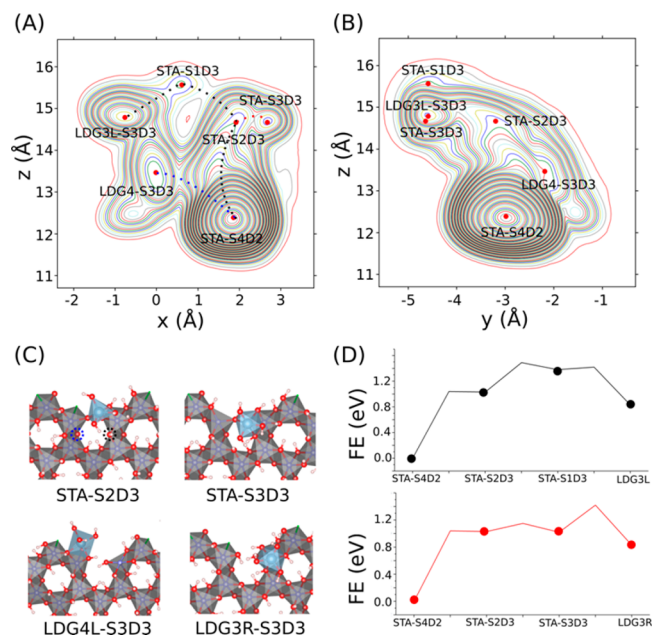


Figure 2. Partial free-energy maps of Al kink site displacement to positions atop ledge sites as a function of (A) *x*- and *z*- and (B) *y*- and *z*-coordinates of a step atom Al. (C) Atomistic models for STA-S2D3, STA-S3D3, LDG4L-S3D3, and LDG3R-S3D3 sites. The Al atom whose coordinates were used as collective variables is shown in cyan, while the other Al atoms are shown in blue. (D) Relative free energies of each site and transition state for the two pathways (black and red lines) drawn in (A). LDG3L-S3D3 and LDG3R-S3D3 are abbreviated as LDG3L and LDG3R.

reaction, the target Al moves upward by breaking one target Al–surface OH bond and one surface Al–surface OH bond to reach the first metastable configuration STA-S2D3 (Figure 2C) defined by a very shallow energy well. In this metastable configuration, Al has become pentacoordinate. However, if two target Al–surface OH bonds break instead, this site becomes STA-S2D2, which is not distinguishable from STA-S2D3 because of their close spatial positions. This first displacement step is unfavorable with a free-energy change of ~ 1.03 eV (Figure 2D). The next step is from the STA-S2D3 site to the tetrahedral STA-S1D3 site with an energy barrier of 0.44 eV. Then, only a small barrier (< 0.04 eV) needs to be overcome for Al to fall into a much more stable adatom site on the ledge, namely, LDG3L-S3D3. The free-energy map for Al displace-

ment from the step edge to the right side of the ledge is similar to that described for the left side (Figure 2D).

The different pathways between the left and right sides of the vacancy can be explained by the different terminations exposed on each side. Specifically, the doubly bound surface OH on the right side, protruding outward (the black dashed circle in Figure 2C), facilitates the transition from STA-S2D3 to STA-S3D3, while the similar OH on the left (the blue dashed circle in Figure 2C) points inward. The last step for Al is to move from the STA-S3D3 site to an adatom site LDG3R-S3D3, crystallographically equivalent to site LDG3L-S3D3, with an energy barrier of 0.40 eV.

Besides adatoms atop the ledge, it is also possible for Al to form adatom sites attached to the side of the ledge (LDG4L-S3D3 of Figure 2C) but hanging below other ledge adatom sites. This transition from STA-S4D2 to LDG4L-S3D3 has an energy barrier of 1.23 eV, about 0.2 eV higher than that from STA-S4D2 to STA-S2D3. In this transition, the target Al breaks one bond with surface OH first and then bonds to another step OH before breaking another bond to surface OH to reach the step adatom site LDG4L-S3D3. In other words, during the process, the coordination number changes from six (STA-S4D2) to five (STA-S3D2) and then back to six (transition state and LDG4L-S3D3).

The migration of Al adatoms away from the ledge onto the terrace involves five symmetrically and energetically inequivalent adatom sites on the ledge and terrace (Figures 3 and S3). These sites are referred to by their adatom site names. LDG2R-S3D2, or LDG2, only exists on the right side of the vacancy. This is because the surface OH underneath of this site is pointing inward, whereas the surface OH at the equivalent site on the left of the vacancy is protruding out of plane. Sites LDG1 and LDG3 are adjacent to LDG2, and all three are close

to the ledge (Figure 3D). Sites TRR1 and TRR2 represent the adatom sites at the interior of the terrace. LDG1, LDG2, and LDG3 are energetically more stable than TRR1 and TRR2, with LDG2 being the most stable site (~ 0.30 eV higher in energy than the step atom site, Figure 3A–C). It is much easier for Al to migrate from LDG1 or LDG3 to LDG2 than the reverse process. The LDG2 \rightarrow LDG3 transition has an energy barrier of 0.65 eV, the largest among those involving ledge sites. It takes 0.50 eV for Al to move from the LDG3 site to the TRR1 site, which is the process of migration from the ledge to the interior of the upper terrace. The migration of Al in the interior of the terrace is composed of the following two processes: TRR1 \leftrightarrow TRR2, with smaller energy barriers (< 0.35 eV). The transition states for all of these processes are similar to a coordination number of five (S2D3). In other words, Al breaks one bond to the surface OH first and then bonds to another surface OH that belongs to another adatom site to complete the six-fold coordination number. On the basis of the relative energies and kinetics of each transition, our results suggest that during step retreat dissolving Al atoms will first aggregate on the ledge and, from there, easily migrate to the interior of the uppermost terraces, leading to two populations of mobile, labile adsorbed species prior to release into solution.

In the third and last process, adatoms detach from ledge or terrace sites into the solution. Here, umbrella sampling calculations were performed to model detachment from the ledge/terrace and formation of a fully solvated outer-sphere (OS) species. We focused on LDG1 and TRR2 as representatives of stable ledge and terrace adatom sites, respectively. Detachment from both sites showed similar energetics and involved similar steps (Figure 4). The first step is from an adatom site (six-fold coordinated) to a S1D3 (four-fold coordinated) configuration, with energy barriers of 0.69 and 0.61 eV for the LDG1 (Figure 4A) and TRR2 (Figure 4B) adatom sites, respectively. Then it takes about 0.30 (LDG1) or 0.36 eV (TRR2) to transition from this tetrahedral configuration to an OS configuration, which is linked to surface hydroxyls through hydrogen bonds. The OS configuration for the LDG1 site is in the form of aluminate, whereas that for TRR2 is a neutral $\text{Al}(\text{OH})_3(\text{H}_2\text{O})_2$.

Once a double kink site has formed, dissolution can proceed via kink propagation. Because sites 1 and 2 close to the double kink site (Figure 1C) have the same coordination number to the surface, both are referred to as kink sites and studied explicitly. From our simulations, the dissolution of kink site 1 (KNK1-S4D2) occurs by a three-process mechanism similar to nucleation of the double kink site (Figure 5A,B). First, Al at the initial edge site breaks one bond with the surface OH and then bonds to another surface OH, resulting in the first metastable intermediate configuration (KNK3-S4D2, Figure 5C). The energy barrier for this step is about 0.56 eV. The next transition is from KNK3-S4D2 to an adatom site (LDG5-S3D3, Figure 5C) by overcoming an energy barrier of 0.46 eV. Al can move from this first ledge adatom site to form a five-coordinated configuration (LDG6-S2D3, energy barrier of 0.22 eV) and then on to a second ledge adatom site (LDG7-S2D3, energy barrier of 0.11 eV). With similar probabilities (energy barrier of 0.27 eV), Al can also migrate to another terrace adatom site (TRR3-S3D3, Figure 5C). Migration from this adatom site to others on the terrace involves adatom configurations and energetics similar to those in TRR1 \leftrightarrow TRR2 transitions. Therefore, it is reasonable to deduce that the energetics of detachment from these adatom sites into the OS

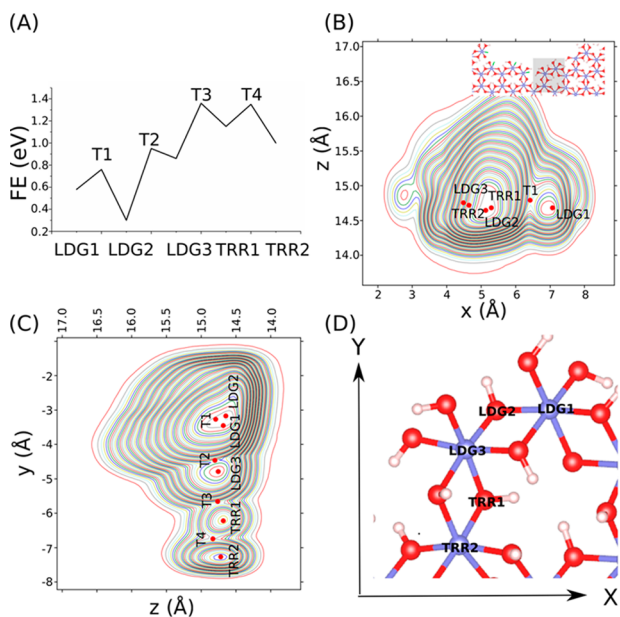


Figure 3. (A) Relative free energies of adatom sites and the transition states. (B) Free-energy map of adatom sites as a function of x - and z -coordinates of the target Al. The area explored in the x - y plane is shaded in gray in the inset and also shown in (D). (C) Free-energy map of adatom sites as a function of y - and z -coordinates. (D) Atomistic model of the (001) surface showing x - y positions of the five adatom sites.

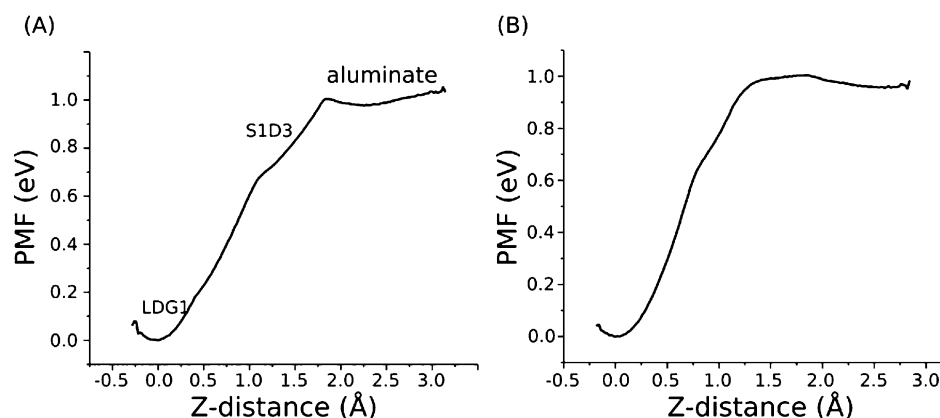


Figure 4. (A) PMF for detachment from the LDG1 site to OS. (B) PMF for detachment from the TRR2 site to the OS. The atomistic models for S1D3 are shown in Figure S3 of the Supporting Information.

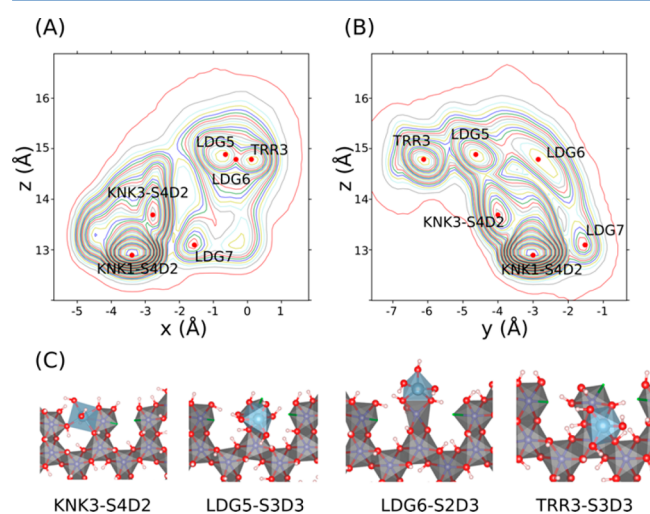


Figure 5. (A) Free-energy map for double kink site 1 formation as a function of x - and z -coordinates of the target Al. (B) Free-energy map for double kink site 1 formation as a function of y - and z -coordinates of the target Al. (C) Atomistic models for KNK3-S4D2, LDG5-S3D3, LDG6-S2D3, and a terrace adatom site (TRR3-S3D3).

configuration is the same as those calculated in the kink site dissolution case.

Similarly, dissolution of kink site 2 shows a tendency to form both ledge and terrace adatoms. The process of Al displacement from kink site 2 to ledge sites involves the movement and deformation of kink site 1. The most energetically uphill process revealed from the free-energy landscape is the move from the double kink site to the first intermediate phase with six-fold coordination (see Figure S4) with an energy barrier of 0.60 eV. When exploring the adatom configurations on the step edge, it is possible for the target Al to substitute the kink site 1, which suggests that kink sites 1 and 2 are interchangeable.

The simulation results allow us to construct a mechanistic model for gibbsite dissolution in basic solutions that underlies the overall mass balance in reaction 1. The two main processes underlying formation and propagation of kinks exhibit a similar three-step mechanism. For the double kink formation, although the transition of Al from a step atom site to a terrace adatom site can occur via multiple pathways, the most likely pathway is via a six-fold coordinated STA-S3D3 configuration, possibly involving the slightly stable intermediate configuration of STA-S2D3. This pathway has an energy barrier of 1.15 eV (or 1.03

eV if the pathway through STA-S2D3 is considered). Another rate-limiting step is the transition from a terrace/ledge adatom to the OS species with a slightly lower energy barrier of ~ 1.0 eV. These predicted energy barriers compare well with the activation energies estimated from temperature-dependent gibbsite dissolution experiments.^{11,18} Therein, regardless of the saturation condition or kinetic model employed in the fit, the activation energies from Arrhenius relationship fits fall in the range of 100–110 kJ/mol (1.04–1.14 eV). We can thus conclude that our simulations may have captured a plausible rate-limiting step for gibbsite dissolution in basic conditions, though further experimental work would be required to test and validate the mechanism.

In that regard, the simulation results provide clues to guide potential experiments aimed at evaluating dissolution mechanisms. Our results suggest that because the dissolving Al can be removed as either $[\text{Al}(\text{OH})_4]^-$ or $\text{Al}(\text{OH})_3(\text{H}_2\text{O})_2$, depending on which part of the terrace it detaches from, dissolution morphology could manifest as a speciation signature in solution. Because aluminate is the only stable species in high pH solutions,²⁴ $\text{Al}(\text{OH})_3(\text{H}_2\text{O})_2$, which has been found to be a stable product of Al hydrolysis at neutral pH,²⁵ will undergo deprotonation. A concentration gradient might therefore form above the surface and be detectable. In addition, our work suggests that the dissolving Al species will initially reside on the ledge but will gradually dissolve into the solution or migrate to the interior of the terrace as the kink site density increases, and therefore, ledge adatom sites become less favorable to occupy. Furthermore, because of the quasi-hexagonal symmetry of the gibbsite basal layer and similar energetics for neighboring kink sites with a similar bonding environment, as suggested from the free-energy maps of both kink sites 1 and 2, step retreat could propagate in multiple directions at nearly the same free-energy decrease, forming a basal surface of mixed low-index step orientations. In Peskeway's AFM work in acidic solution,¹⁹ they observed local (110) and (100) sections that coexisted for the same step during dissolution.

The simulation results highlight some unique features of metal oxide dissolution compared to processes typically involved in the dissolution of ionic crystals. The overall trend of the change of the Al–surface OH coordination number is from 4 to 3 to 1 and finally to 0. However, unlike ionic crystals,³ multiple states are accessible for each coordination number, and the coordination number can change during transitions between those states having the same coordination number.

Another major difference between the previously studied ionic crystal systems and ours is the higher affinity of surface OH for the dissolving Al to complete its six-fold coordination than that of solvent water molecules (ignoring for present purposes the competition from dissolved OH⁻ species in the solution). In addition to a higher bonding energy in covalently bonded crystals, this affinity difference might also explain the slower kinetics of the dissolution of covalently bonded metal oxide crystals.

The growth mechanism, as the reverse process of dissolution, can also be inferred from our results because the reversibility of each step in the free-energy landscape is naturally included in the modeling approach. In contrast to the reverse process, the transition from an OS adsorbed configuration to an adatom on a terrace is facile, requiring only a small energy barrier of 0.06 eV to be overcome. Nutrient migration rates across a terrace close to kink sites would be the same as that involved during dissolution, and these energy barriers are within the range of 0.2–0.4 eV. The next step of transition from an adatom site to kink site is more complex. Although we have not explicitly conducted rigorous tests of reversibility in this study, it is suggested from the free-energy maps that ledge adatoms are likely energetically favorable and can be used as an alternative docking location for the addition of the next monomer for growth by step edge advance. Also, because docking locations at ledges can entail metastable pentacoordinate Al, this conceptual model for growth is consistent with recent NMR measurements showing that this minor species is indeed involved in the crystallization of gibbsite from aqueous solution.²⁶

Our model predicts the first overall free-energy landscape for the multistep dissolution of an important metal oxide, providing some mechanistic insights for future studies of OH⁻ concentration effects on these individual reactions and guidelines for prospective higher-level simulations (e.g., density functional theory) to test the sensitivity of force fields in predicting these individual states and reactions. Transmission coefficients for the pathways revealed in this work will be calculated to account for the recrossings of transition states and to more comprehensively determine the rates. In addition, the role of counterions used in dissolution experiments such as Na⁺ would be worth examining explicitly as Na⁺ could strongly adsorb on the gibbsite surfaces.²⁷ The adsorbed Na⁺ on the surface could attract the hydroxyls that belong to the dissolving Al polyhedra, favoring the dissolution. Furthermore, fewer surface hydroxyls are accessible to the dissolving Al due to screening and/or steric interference by the adsorbed Na⁺, and thus, fewer adatom sites are accessible, which might also increase the dissolution rate.

■ ASSOCIATED CONTENT

● Supporting Information

The Supporting Information is available free of charge on the ACS Publications website at DOI: [10.1021/acs.jpcllett.8b00484](https://doi.org/10.1021/acs.jpcllett.8b00484).

Further computational details and analyses, including force field parameters, modified Al–OH potential, force field benchmarking against aluminum hydroxide bulk structures and aqueous aluminate ion structure, free-energy calculation details, comparison in the stability of an in-plane interstitial site between DFT and force fields, atomistic models for states mentioned but not shown in

the main text, and free-energy map for kink site 2 dissolution ([PDF](#))

■ AUTHOR INFORMATION

Corresponding Authors

*E-mail: zhizhang.shen@pnnl.gov (Z.S.).

*E-mail: Kevin.Rosso@pnnl.gov (K.M.R.).

ORCID

Zhizhang Shen: 0000-0002-8837-5573

Sebastien N. Kerisit: 0000-0002-7470-9181

Andrew G. Stack: 0000-0003-4355-3679

Kevin M. Rosso: 0000-0002-8474-7720

Notes

The authors declare no competing financial interest.

■ ACKNOWLEDGMENTS

This work was supported by IDREAM (Interfacial Dynamics in Radioactive Environments and Materials), an Energy Frontier Research Center funded by the U.S. Department of Energy (DOE), Office of Science, Basic Energy Sciences (BES). The research was performed using PNNL Institutional Computing at Pacific Northwest National Laboratory (PNNL). PNNL is a multiprogram national laboratory operated for DOE by Battelle Memorial Institute under Contract No. DE-AC05-76RL0-1830. The authors gratefully acknowledge fruitful discussions with Xin Zhang regarding experimental observations of gibbsite dissolution and Micah Prange regarding DFT simulations setup.

■ REFERENCES

- (1) Stumm, W.; Morgan, J. J. *Aquatic Chemistry*; Genium Publishing Corporation: Schenectady, NY, 1996.
- (2) Casey, W. H.; Westrich, H. R.; Banfield, J. F.; Ferruzzi, G.; Arnold, G. W. Leaching and Reconstruction at the Surfaces of Dissolving Chain-Silicate Minerals. *Nature* **1993**, *366*, 253–256.
- (3) Stack, A. G.; Raiteri, P.; Gale, J. D. Accurate Rates of the Complex Mechanisms for Growth and Dissolution of Minerals Using a Combination of Rare-Event Theories. *J. Am. Chem. Soc.* **2012**, *134*, 11–14.
- (4) De La Pierre, M.; Raiteri, P.; Stack, A. G.; Gale, J. D. Uncovering the Atomistic Mechanism for Calcite Step Growth. *Angew. Chem., Int. Ed.* **2017**, *56*, 8464–8467.
- (5) Spagnoli, D.; Kerisit, S.; Parker, S. C. Atomistic Simulation of the Free Energies of Dissolution of Ions from Flat and Stepped Calcite Surfaces. *J. Cryst. Growth* **2006**, *294*, 103–110.
- (6) Raiteri, P.; Demichelis, R.; Gale, J. D. Thermodynamically Consistent Force Field for Molecular Dynamics Simulations of Alkaline-Earth Carbonates and Their Aqueous Speciation. *J. Phys. Chem. C* **2015**, *119*, 24447–24458.
- (7) Joswiak, M. N.; Doherty, M. F.; Peters, B. Ion Dissolution Mechanism and Kinetics at Kink Sites on NaCl Surfaces. *Proc. Natl. Acad. Sci. U. S. A.* **2018**, *115*, 656.
- (8) Leung, K. First-Principles Modeling of Mn(II) Migration above and Dissolution from Li_xMn₂O₄ (001) Surfaces. *Chem. Mater.* **2017**, *29*, 2550–2562.
- (9) Benedek, R.; Thackeray, M. M.; Low, J.; Bučko, T. Simulation of Aqueous Dissolution of Lithium Manganate Spinel from First Principles. *J. Phys. Chem. C* **2012**, *116*, 4050–4059.
- (10) Pearson, T. G. *The Chemical Background of the Aluminium Industry (Lectures and Monographs)*; Royal Institute of Chemistry, 1955; Vol. 3, p 103.
- (11) Pereira, J. A. M.; Schwaab, M.; Dell’Oro, E.; Pinto, J. C.; Monteiro, J. L. F.; Henriques, C. A. The Kinetics of Gibbsite Dissolution in NaOH. *Hydrometallurgy* **2009**, *96*, 6–13.

(12) Gimpel, R. F.; Reynolds, D. A. Determining Aluminum Compounds and Amounts in Hanford Tank Waste. *Proceedings of the 12th International High-Level Radioactive Waste Management Conference*; 2008; pp 744–748.

(13) Krupka, K. M.; Cantrell, K. J.; Schaef, H. T.; Arey, B. W.; Heald, S. M.; Deutsch, W. J.; Lindberg, M. J. Characterization of Solids in Residual Wastes from Single-Shell Tanks at the Hanford Site, Washington, USA. *Radwaste Solut. Mag.* **2010**, *17* (ANL/XSD/JA-66013).

(14) Peterson, R. A.; Buck, E. C.; Chun, J.; Daniel, R. C.; Herting, D. L.; Ilton, E. S.; Lumetta, G. J.; Clark, S. B. Review of the Scientific Understanding of Radioactive Waste at the US DOE Hanford Site. *Environ. Sci. Technol.* **2018**, *52*, 381–396.

(15) Bénézech, P.; Palmer, D. A.; Wesolowski, D. J. Dissolution/Precipitation Kinetics of Boehmite and Gibbsite: Application of a pH-Relaxation Technique to Study near-Equilibrium Rates. *Geochim. Cosmochim. Acta* **2008**, *72*, 2429–2453.

(16) Scotford, R. F.; Glastonbury, J. R. Effect of Temperature on the Rates of Dissolution of Gibbsite and Boehmite. *Can. J. Chem. Eng.* **1971**, *49*, 611–616.

(17) Scotford, R. F.; Glastonbury, J. R. The Effect of Concentration on the Rates of Dissolution of Gibbsite and Boehmite. *Can. J. Chem. Eng.* **1972**, *50*, 754–758.

(18) Grénman, H.; Salmi, T.; Murzin, D. Y.; Addai-Mensah, J. The Dissolution Kinetics of Gibbsite in Sodium Hydroxide at Ambient Pressure. *Ind. Eng. Chem. Res.* **2010**, *49*, 2600–2607.

(19) Peskleyway, C. D.; Henderson, G. S.; Wicks, F. J. Dissolution of Gibbsite: Direct Observations Using Fluid Cell Atomic Force Microscopy. *Am. Mineral.* **2003**, *88*, 18–26.

(20) Kurganskaya, I.; Lutge, A. Kinetic Monte Carlo Approach To Study Carbonate Dissolution. *J. Phys. Chem. C* **2016**, *120*, 6482–6492.

(21) Cygan, R. T.; Liang, J.-J.; Kalinichev, A. G. Molecular Models of Hydroxide, Oxyhydroxide, and Clay Phases and the Development of a General Force Field. *J. Phys. Chem. B* **2004**, *108*, 1255–1266.

(22) Stack, A. G. Next Generation Models of Carbonate Mineral Growth and Dissolution. *Greenhouse Gases: Sci. Technol.* **2014**, *4*, 278–288.

(23) Liu, X.; Lu, X.; Sprik, M.; Cheng, J.; Meijer, E. J.; Wang, R. Acidity of Edge Surface Sites of Montmorillonite and Kaolinite. *Geochim. Cosmochim. Acta* **2013**, *117*, 180–190.

(24) Sipos, P. The Structure of Al(III) in Strongly Alkaline Aluminate Solutions - A Review. *J. Mol. Liq.* **2009**, *146*, 1–14.

(25) Kubicki, J. D. Self-Consistent Reaction Field Calculations of Aqueous Al^{3+} , Fe^{3+} , and Si^{4+} : Calculated Aqueous-Phase Deprotonation Energies Correlated with Experimental $\ln(K_a)$ and $\text{p}K_a$. *J. Phys. Chem. A* **2001**, *105*, 8756–8762.

(26) Hu, J. Z.; Zhang, X.; Jaegers, N.; Wan, C.; Graham, T. R.; Hu, M. Y.; Pearce, C. I.; Felmy, A. R.; Clark, S. B.; Rosso, K. M. Transitions in Al Coordination During Gibbsite Crystallization Using High-Field ^{27}Al and ^{23}Na MAS NMR Spectroscopy. *J. Phys. Chem. C* **2017**, *121*, 27555–27562.

(27) Shen, Z.; Ilton, E. S.; Prange, M. P.; Kerisit, S. N. Molecular Dynamics Simulations of the Interfacial Region between Boehmite and Gibbsite Basal Surfaces and High Ionic Strength Aqueous Solutions. *J. Phys. Chem. C* **2017**, *121*, 13692–13700.